Yousaf Shah, M.A.K.; Lu, Yuzheng; Mushtaq, Naveed; Yousaf, Muhammad; Akbar, Muhammad; Rauf, Sajid; Dong, Yiwang; Lund, Peter; Zhu, Bin; Asghar, Imran

Enabling high ionic conductivity in semiconductor electrolyte membrane by surface engineering and band alignment for LT-CFCs

Published in:
Journal of Membrane Science

DOI:
10.1016/j.memsci.2022.121264

Published: 01/02/2023

Document Version
Publisher's PDF, also known as Version of record

Journal of Membrane Science 668 (2023) 121264

Contents lists available at ScienceDirect

Journal of Membrane Science

journal homepage: www.elsevier.com/locate/memsci

Enabling high ionic conductivity in semiconductor electrolyte membrane by surface engineering and band alignment for LT-CFCs

M.A.K. Yousaf Shah [a,1], Yuzheng Lu [b,**,1], Naveed Mushtaq [a], Muhammad Yousaf [a], Muhammad Akbar [e], Sajid Rauf [c], Yiwang Dong [f], Peter D. Lund [a,d], Bin Zhu [a,***], Muhammad Imran Asghar [d,e,*]

[a] Jiangsu Provincial Key Laboratory of Solar Energy Science and Technology/Energy Storage joint Research Center, School of Energy and Environment, Southeast University, No.2 Si Pai Lou, Nanjing, 210096, China
[b] School of Electronic Engineering, Nanjing Xiao Zhuang University, 211171, Nanjing, China
[c] College of Electronics and Information Engineering, Shenzhen University, Guangdong Province, 518000, China
[d] New Energy Technologies Group, Department of Applied Physics, Aalto University School of Science, P. O. Box 15100, FI-00076, Aalto, Espoo, Finland
[e] Faculty of Physics and Electronic Science, Hubei University, Wuhan, Hubei, 430062, China
[f] School of Electrical Engineering and Automation, Wuhan University, Wuhan, 430072, Hubei Province, China

ARTICLE INFO

Keywords:
Ceramic fuel cells
Surface doping
High proton conduction
Energy band alignment

ABSTRACT

Wide bandgap semiconductor perovskite $SrTiO_3$ (STO) has attracted extensive attention due to its higher kinetics of electrons (electronic conductivity). However, rare studies have been performed to tune the STO semiconductor towards ionic conduction, which could make it a promising candidate for an electrolyte in ceramic fuel cells (CFCs). Herein, we have designed a semiconductor perovskite Co/Fe–$SrTiO_3$ as an electrolyte membrane to tune its semiconducting property to the ionic conduction via surface-enriched O-vacancies. The surface doping of Co/Fe into $SrTiO_3$ resulted in lowering the Fermi level, leading to the space charge region and local electric field on the surficial region, which can enhance the ionic conduction (proton conduction) at the surface. The designed electrolyte exhibited a high ionic conductivity of 0.19 S/cm and the fuel cell employing it delivered a maximum power density of 1016 mW/cm^2 at 520 °C. Moreover, the theoretical calculation was performed to support the experimental results, like disorder in lattice and oxygen vacancy formation energy. The surface doping of Co/Fe facilitated the enriched surface channels for quick ion transportation with lower activation energy. The presented methodology of surface doping has proven to be suitable for designing advanced materials for wide bandgap semiconductors with high ionic conductivity to develop next-generation CFCs.

1. Introduction

Ceramic fuel cells (CFCs), like solid oxide fuel cells (SOFCs) or proton ceramic fuel cells (PCFCs), have attracted extensive attention worldwide [1]. However, the commercialization of the traditional electrolyte YSZ-based SOFC is limited due to its high operating temperature (above 800 °C), which causes several material and degradation issues resulting in high-cost of the system. Therefore, reducing the operating temperature (400–650 °C) yet with reasonable power output is the most crucial step to realize the large scale SOFCs commercialization [2,3]. Also, developing electrolytes with high ionic conduction becomes a new trend to realize the SOFCs at low operational temperatures. So extensive efforts have been made to design and optimize electrolytes to reach sufficient ionic conductivity, but only a few approaches remain successful in attaining 0.1 S/cm [2,4–6]. Although recent studies in the literature reported PCFCs which could be operated at lower temperatures (350–700 °C), the ionic conductivity of the proton conducting perovskite oxides used in the cells, $BaZrO_3$ and $BaZrCeO_3$, is quite low (10^{-3} to

* Corresponding author. New Energy Technologies Group, Department of Applied Physics, Aalto University School of Science, P. O. Box 15100, FI-00076, Aalto, Espoo, Finland.
** Corresponding author.
*** Corresponding author.
E-mail addresses: mrluyuzheng@163.com (Y. Lu), zhu-bin@seu.edu.cn (B. Zhu), imran.asghar@aalto.fi (M.I. Asghar).
[1] These authors have contributed equally.

https://doi.org/10.1016/j.memsci.2022.121264
Received 23 September 2022; Received in revised form 2 November 2022; Accepted 2 December 2022
Available online 5 December 2022

10^{-2} S/cm at 600 °C) [7–10].

From the other perspective, lately semiconductor materials with extrinsic electronic conductivity, including $LiCo_{0.5}Al_{0.5}O_2$, $SrTiO_3$, $SmNiO_3$, CeO_2, and TiO_2, have been used to realize the low-temperature operation of CFCs due to transport of either proton or oxide ions in the cells [11–17]. The CFCs electrolyte should have sufficient ionic conductivity to transport ions to complete the (H_2 at the anode, O_2 at the cathode side) electrode reaction (redox reaction) to maintain a reasonable power output. In addition, the CFC electrolytes must have a negligible electronic conductivity to block any electronic leakage through the cell; but the semiconductor materials possess intrinsic electronic conductivity [18]. To overcome this limitation, a new methodology of energy band alignment has been developed for tuning the semiconducting property, especially for wide bandgap oxides, to ionic conduction [18,19].

$SrTiO_3$ is a typically n-type semiconductor with a wide bandgap of 3.2 eV. It has been used widely for solar cells, batteries, photocatalysis, and fuel cell applications due to its enormously enriched electrical, physical, and optical properties [20]. Also, doping different elements, especially the lower valent such as the Al^{+3}, La, Nb, Fe, etc., into $SrTiO_3$ remains a practical approach to enhance the performance by producing abundant O-vacancies of different devices, including photocatalysis and fuel cell [21–25]. Also, in recent years the heterostructure technique has emerged as an exciting area in boosting the performance of fuel cells [26,27]. A series of studies have been conducted on STO/YSZ (semiconductor-ionic) planar heterostructure, revealing eight orders of magnitude higher ionic conductivity than the individual YSZ, which shows the importance of a heterostructure approach for electrolyte synthesis [28]. Later, Xia et al. designed a bulk semiconductor ionic heterostructure of STO-SDC to exhibit a remarkable fuel cell performance of 892 mW/cm^2 and high ionic conductivity of 0.14 S/cm at a low operating temperature of 550 °C [29]. In another study, $SrTiO_3$ has been used as an electrolyte to deliver a reasonable fuel cell performance of 620 mW/cm^2 and a high ionic conductivity of 0.24 S/cm at 550 °C. A core-shell structure was proposed for the straightforward pathway of protons and oxide ions due to the formation of $LiCO_3$ between the surface and interface region [12]. Gang et al. proposed a novel approach to core-shell structure to enable superionic surface conduction by designing a new semiconductor perovskite electrolyte $La_{0.25}Sr_{0.75}TiO_3$ to deliver better fuel cell performance of 908 mW/cm^2 along with superoxide ion conduction of 0.22 S/cm at 550 °C. The formed heterostructure between the insulating core and superionic conducting surface layer (shell) where a surface layer or grain boundary is recognized as the primary source for the fast ions transportation [22]. In addition, many perovskite materials like Sm-NiO have been used as electrolytes to deliver a good fuel cell performance and benefitted from the mott-transition phenomena to suppress electronic conduction [13].

Moreover, many heterostructure-based devices have been designed to suppress the electronic conductivity while enhancing ionic conduction mainly due to the formation of heterojunctions like BCFZY-ZnO (p-n junction), delivering excellent fuel cell performance and higher ionic conductivity with diminished electronic conduction [30]. Also, the above studies revealed that the construction of heterostructure constitutes LEF (local electric field), which causes creation of an excess number of O-vacancies on the surface layer. This high concentration of O-vacancies enhances the surface ionic (proton) conduction significantly. Therefore, the $SrTiO_3$-based junction structure could be an efficient and effective strategy to empower the flow of ions by constructing the interfacial region.

In our current work, we have designed the CF-$SrTiO_3$ (prepared via the surface doping of Co/Fe into $SrTiO_3$) to investigate its ionic conduction properties as an electrolyte for LT-CFC. The Co and Fe surface doping lowers the Fermi level of $SrTiO_3$ leading to redistribution of charges at the interface to build the space charge region, which finally constitutes the local electric field (LEF) at the interface. Surface doping causes the creation of enriched O-vacancies on the surface where the construction of a junction could enable the highways of ions (protons) transport through the constituted LEF. Experimental studies (XRD, HR-TEM, XPS, Raman, and Energy band alignment) reveal that surface doping is beneficial for enhancing ionic conduction. The designed electrolyte 10%CF-$SrTiO_3$ produced an outstanding fuel cell performance of 1016 mW/cm^2 along with high ionic conductivity of 0.19 S/cm suggesting that constructed electrolyte material is a potential candidate for CFC application.

2. Experimental section

2.1. Powder preparing and characterization

The CF-$SrTiO_3$ electrolyte powder was synthesized using the surface doping technique assisted by the sol-gel method. In detail, the $Co(NO_3)_2$ and $Fe(NO_3)_2$ and commercially prepared $SrTiO_3$ were used in the preparation of 10%CF-$SrTiO_3$ ($SrCo_{0.1}Fe_{0.1}TiO_3$) electrolyte. At first, sol of $Co(NO_3)_2$ and $Fe(NO_3)_2$ was prepared in one beaker with 200 ml of deionized water and leave it to stir for proper mixing. Afterwards, the appropriate amount of citric acid was mixed in the above solution to work as a chelating agent. The ratio between the precursors and the chelating agent was 1:1. The commercially available material $SrTiO_3$ with the appropriate amount of 0.9 g/m was poured into the solution of Co and Fe nitrates and was kept on stirring. Afterwards, the final solution was heated at 80 °C and stirred until the gel was formed. After the formation of the gel, the temperature was increased to 100 °C for firing and drying the final materials.

Consequently, the combusted solution was placed in a heating furnace at 120 °C (overnight) to dry the ultimate solution. The dried solution was grounded and set for sintering at 700 °C for 3 h at 3 °C/min to obtain the final product of 10%CF-$SrTiO_3$. The other composition, 5% CF-$SrTiO_3$ and 15%CF-$SrTiO_3$, was prepared similarly to the earlier solution.

The XRD analysis with the source of Cu kα $\lambda = 1.54060$ Å radiation assisted with tube voltage and current of 45 kV and 40 mA was used to investigate the structural phase of synthesized powder of 10%CF-$SrTiO_3$ & 5%CF-$SrTiO_3$. The 2θ-range of 20–80° was chosen to collect the XRD data. The powder morphology of 10%CF-$SrTiO_3$ & 5%CF-$SrTiO_3$ was investigated using FE-SEM (Field emission-scanning electron microscopy, Hitachi Regulus8100). Consequently, deep and detailed microstructure morphology was inspected by employing the accelerating voltage of 200 kV using transmission electron microscopy (TEM, JEOL JEM-2100F). Also, individual element mapping of synthesized material was performed using the EDS mapping, and line scanning assisted with HR-TEM.

Furthermore, to investigate the surface charge transportation and chemical state XPS (x-ray photoelectron spectroscopy). In addition, Origin and CASA XPS software were used to fit and analyze the XPS data. The energy bandgap and valence band were evaluated using the Uv–visible spectroscopy and UPS (ultra-photoelectron spectroscopy) spectra to construct the energy band structure. Raman Spectra of as-prepared powder of 10%CF-$SrTiO_3$ & 5%CF-$SrTiO_3$ were measured using a 532 nm beam commenced Raman microscope (Lab RAM HR 800 UV, Horiba Jobin Yvon, France).

2.2. Fuel cell assembly and measurements

The symmetrical electrodes Ni-NCAL ($Ni_{0.8}Co_{0.15}Al_{0.05}LiO_{2-\delta}$) and synthesized electrolyte powder 10%CF-$SrTiO_3$ & 5%CF-$SrTiO_3$ and other compositions were used to prepare the pellet by compressing the electrolyte between two symmetrical electrodes Ni-NCAL like a sandwich. The 250 MPa pressure was applied for pressing the sandwiched-like pellet configuration of Ni-NCAL/10%CF-$SrTiO_3$ & 5%CF-$SrTiO_3$/NCAL-Ni and sustaining the applied pressure for 2-mints to obtain the button shape pellet. Later the Pellet was extracted from the mould and fixed in the testing device for electrical and electrochemical studies. The

button shape pellet's active area and diameter were 0.64 cm^2 and 13 mm. The constructed button shape pellet thickness was 1.5 mm, and the electrolyte layer thickness was 760 μm. Before the fuel cell measurements, the constructed cell with the configuration of (Ni-NCAL/10%CF-$SrTiO_3$ & 5%CF-$SrTiO_3$/NCAL-Ni) was sintered at 650 for 2 h.

Moreover, three more pellets of 10%CF-STO were prepared in the same way to test the reproducibility of fuel cell performance. The Ni-NCAL electrodes, either the anode or the cathode, were prepared using commercial NCAL powder, Ni foam, and terpinol liquid. Initially, the NCAL powder was grounded then an appropriate amount of terpineol was poured into the NCAL powder and mixed to gain the NCAL slurry.

On the other hand, the button shape of Ni-foam was cut. Later, the prepared slurry of NCAL was transformed into the Ni-foam by pasting the NCAL using a brush to cover the whole surface of the Ni-foam. Afterwards, the Ni-foam pasted NCAL electrodes were dried at 120° for 20 min to attain the Ni-NCAL electrodes (anode & cathode).

Afterwards, the pellet was fixed in the testing device to run the fuel cell performance and impedance spectroscopy. A pressure of 80–120 ml min^{-1} and 150–200 ml min^{-1} was used to supply the hydrogen and air to the cell, where hydrogen was delivered to the anode side while the air was purged to the cathode side to run the electrochemical reaction. The programmable electronic load (IT8511) was used to perform the fuel cell performance and to collect the current and voltage reading. Further, the obtained data were plotted using the Origin software. The electrochemical impedance spectroscopy (EIS) analysis was performed using the electrochemical workstation of Gamry, 3000, where EIS was completed in an H_2/Air environment at 520-420 °C. The applied frequency was set in the range of 0.1 HZ to 1 MHZ with an amplitude of 10 mV.

2.3. DFT calculation

The spin-polarized DFT calculation was carried out using the (CASTEP) of material studio 8.0 for Optimization. A plane wave with a cut-off energy of 520 eV was applied to expand the valence electron of Sr $4s^2$ $4p^6$ $5s^2$, Co 3 d^7 $4s^2$, Fe 3 d^6 $4s^2$, Ti $3s^2$ $3p^6$ 3 d^2 $4s^2$ and O $2s^2$ $2p^4$. GGA (generalized gradient approximation) with PBE (Perdew-Burke-Ernzerhof) function was applied to investigate the ion and electron-electron interaction. 3 × 3 × 3 k point grid Brillion zone structure with 143 atoms is utilized in the current study. To improve the calculation accuracy, U_{eff} = U-J = 4.5 was applied in our study, which is normally used for transition metals. The 10^{-5} and 0.02 eV/Å are the force and energy for convergence. The oxygen vacancy formation energy was calculated using the following equation.

$$E\ddot{V}_o = E_{tot}(V_O^q) - E_{tot}(ideal) + \mu + q(E_F + E_{valan} + \Delta V)$$

The detailed parameters of the above equation can be found elsewhere [31–33].

3. Result & discussion

Fig. 2(a) reveals the room-temperature acquired XRD pattern of 10% CF-$SrTiO_3$ & 5%CF-$SrTiO_3$ electrolyte materials. Based on the obtained

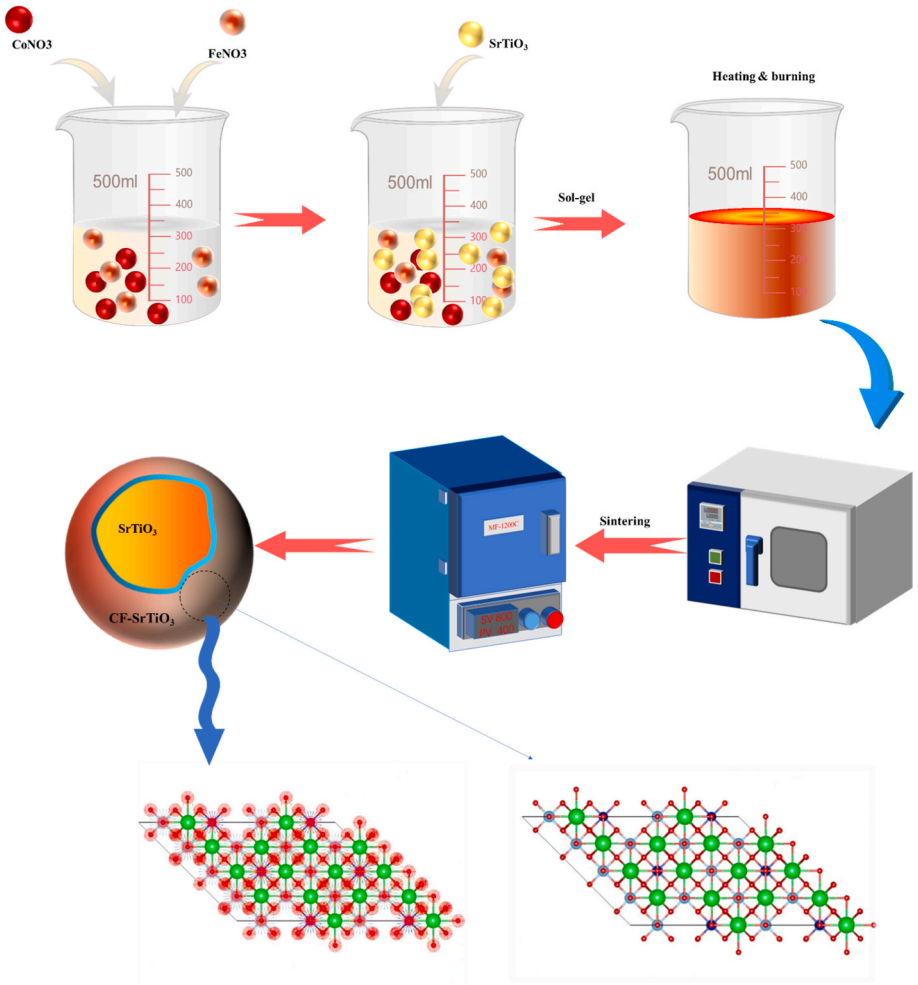

Fig. 1. Schematic diagram of synthesis procedure of CF-$SrTiO_3$ powder along with the structure of CF-$SrTiO_3$ in a-b plane (dotted Surface and bulk).

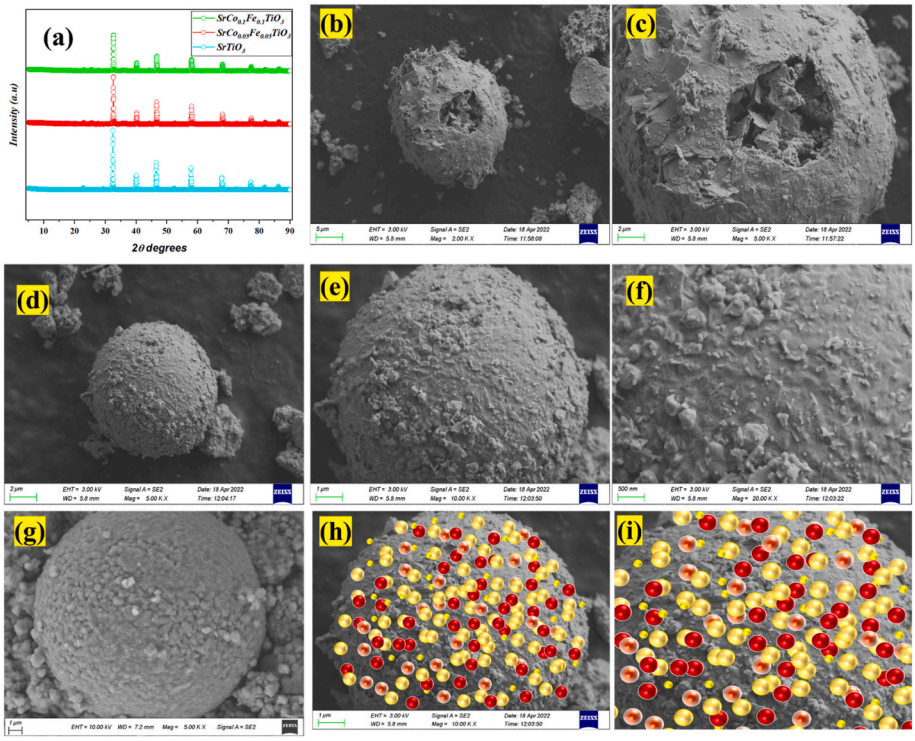

Fig. 2. (a) XRD pattern of $SrTiO_3$, 5%CF-$SrTiO_3$ and 10%CF-$SrTiO_3$, (b, c) SEM images of 5% CF-$SrTiO_3$ with different magnification scale 5-2 μm, (d–f) the SEM images of 10%CF-$SrTiO_3$ with different resolution scale 2 μm, 1 μm and 500 nm, (g) is the SEM image of NCAL electrode while (h, i) is the particle distribution of Fe and Co on the surface of $SrTiO_3$.

data, the XRD pattern of 10%CF-$SrTiO_3$ & 5%CF-$SrTiO_3$ mostly cross-ponds to cubic perovskite structure; a minor peak of Co/Fe is apparent due to the low-temperature sintering suggesting that the obtained structure is pure cubic perovskite structure; also, it is in agreement with the published literature [12,23,34]. The surface doping content of 5% and 10% were used in pure $SrTiO_3$ crystalline structure, and the doping caused enhanced the lattice parameters and reduce the peak intensity. Also, peaks shifting appeared, which might be due to the different ionic radii of Fe, Co, and Ti following Vegard's law [24,35]. Also, surface dopants can change the valence state of the host material, leading to charge compensation and lattice expansion. According to the phase, the lattice parameter was calculated using the afore-reported equation named sherr-equation $D = K\lambda/L(\cos\theta)$. The lattice parameters for 10% CF-$SrTiO_3$ & 5%CF-$SrTiO_3$ are 3.879 Å and 3.89605 Å. The obtained data confirmed the statement described above related to the lattice parameter. Co and Fe surface doping experienced lattice expansion, as demonstrated in the XRD result. A separated image of XRD is shown in the Supplementary information (Fig.SI (1, 2)). Moreover, XRD, after testing, was analyzed which confirmed the pure perovskite structure of the crystals. The XRD results before and after test have been illustrated in supplementary information (Fig.SI (3(a, b)).

According to the SEM (scanning electron microscopy), the particles of 10%CF-$SrTiO_3$ & 5%CF-$SrTiO_3$ where Co and Fe are surfaces doped into $SrTiO_3$ are sintered at 700° for 3 h, appear in the range of 5, 2, 1 μm and 500 nm as displayed in Fig. 2(b–f). The particles of 10%CF-$SrTiO_3$ & 5%CF-$SrTiO_3$ appeared in the shape of balls where particles of Co and Fe are in-homogeneously distributed at the micro level in the STO lattice. In contrast, particle distribution at the nanoscale seems to be consistent. Moreover, particles seem to be well-doped, suggesting that surface doping of Co and Fe enhances the surface area with enriched active states leading to enhanced diffusion of charges at the surface. The interlinked surface particles or network of surface particles tremendously favour improving the performance of fuel cell devices which needs to be debated in a later section [27]. Fig. 2 (g) shows the particle of electrode NCAL revealing the porosity and uniformity, which could be beneficial for better catalytic activity. Further, Fig. 2(h and i) shows the particle's uniform distribution; all particles have been displayed in different colours, where yellow resembles the $SrTiO_3$ while orange and red are related to the Fe and Co.

Furthermore, HR-TEM of 10%CF-$SrTiO_3$ & 5%CF-$SrTiO_3$ reveals the detailed microstructure at nanoscale 100-5 nm, revealing that Co and Fe are dispersed on the Surface of $SrTiO_3$ particles as shown in Fig. 3(a–d). Also, Fig. 3(c and d) reveals that a well and strong diffraction plane has been confirmed, suggesting the well crystalline structure and well-aligned with the XRD phase structure; the existence of the surface layer confirmed the surface doping of Co/Fe into $SrTiO_3$ lattice. Moreover, the particles at nanoscales with more active sites seem to be well-adherent and coherent, establishing a series of connections between particles, further enhancing the charge transportation at the surface and interface [17,23,27]. The diffraction planes with different d-spacing 0.24 nm and 0.26 nm cross-ponds to the diffraction planes of 110 101, respectively. Fig. 3(e) shows the SAEED pattern of 10%CF-$SrTiO_3$, revealing the planes in circular shapes; each circle has been assigned to a specified and substantial diffraction plane.

Moreover, the HR-TEM elemental mapping of each element was inspected by considering the image with constituent color, as shown in Fig. 3(f). The EDS mapping and line scanning confirm the presence of each element, including Sr, Co, Fe, Ti, and O, as displayed in Fig. 3(g–l). The mapping and line scanning reveal that all elements are uniformly distributed in the proposed composition of 10%CF-$SrTiO_3$, where Co and Fe are dispersed on the surface $SrTiO_3$, indicating the enrichment of surface area, and creating a more active site which overall benefits the performance of the fuel cell. Furthermore, more precise and separate images of SEM and HR-TEM along with EDS line scanning are presented in supporting information (Fig SI. (4–6)).

EIS analysis was performed to investigate the electrical characteristics of proposed materials $SrTiO_3$, 10%CF-$SrTiO_3$ & 5%CF-$SrTiO_3$. The EIS analysis was performed under different gas environments, H_2 and

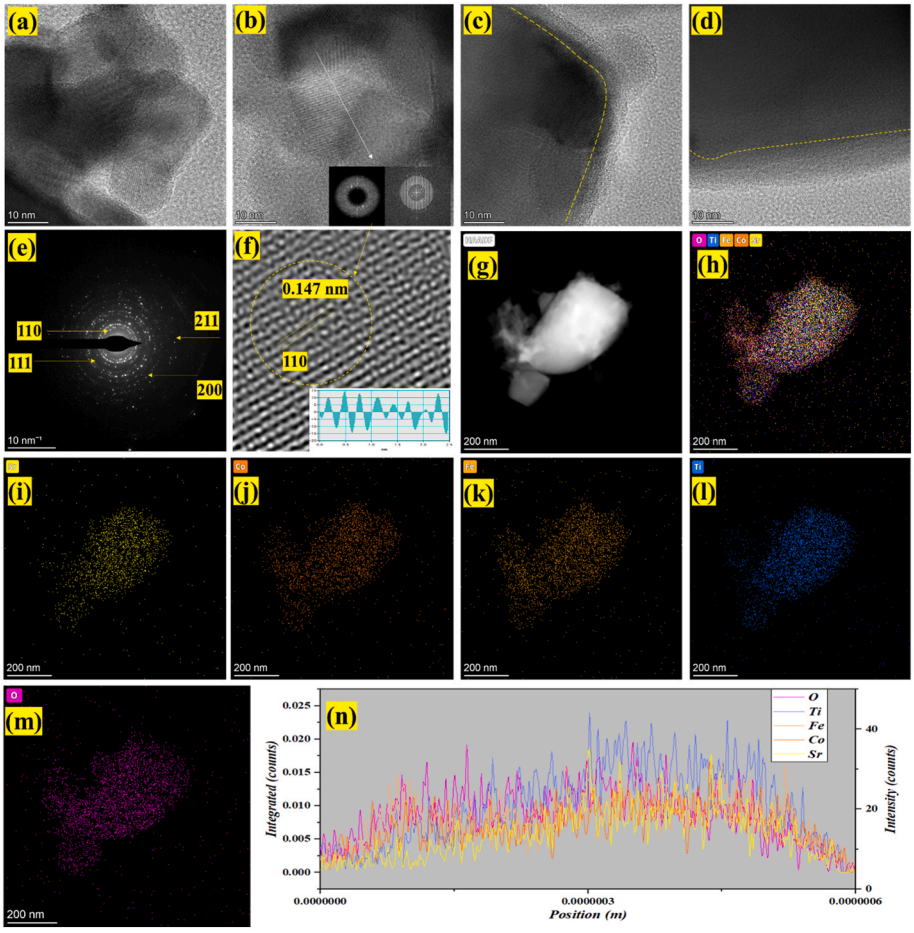

Fig. 3. (a–d) HR-TEM images of 10%CF-$SrTiO_3$ revealing the surface layer due to surface doping, (e, f) Saeed pattern of 10%CF-$SrTiO_3$ with circular rings and diffraction plane of (110) with d-spacing of 0.147 nm, (g, h) HAADF image of 10%CF-$SrTiO_3$ and colourful image constituting all elements, (i–m) elemental mapping of all elements including Sr, Co, Fe, Ti, and O while (n) is the line scanning of 10%CF-$SrTiO_3$.

Air, and at different operational temperatures of 520-420 °C, as depicted in Fig. 4(a–c). The Ohmic and electrode polarization resistance of EIS curves were recorded under the change of frequency at different temperatures of 520-420 °C. The intersection point on the real axis is known as the starting point or high-frequency point, which usually corresponds to the ohmic resistance and can be denoted as R_o. Also, two more semicircles affiliated with the intermediate and lower frequency regions correspond to the charge and mass transfer processes [15,17,30]. Fig. 4 (d) shows the EIS spectra of five-layer (Ni-NCAL/BZY/CF--STO/BZY/NCAL-Ni) under H_2/Air environment at 520-420 °C. Also, the EIS curve was fitted using the ZSIMPWIN software by employing the equivalent circuit LR_o (R_1Q_1) (R_2Q_2), and fitted data have been formulated in Table SI. (1–2). The R_1 and R_2 correspond to the polarization resistance and can be denoted as R_p. The ohmic and polarization resistance of 10%CF-$SrTiO_3$ is lower than $SrTiO_3$ and 5%CF-$SrTiO_3$. The polarization resistance combines R_1 and R_2, as presented in Table SI. (1–2).

In detail, the R_1 manifests the resistance between the electrode and electrolyte interface for the transportation of ions. In contrast, R_2 signifies the adsorption and dissociation process for the oxygen ion. The R_o and R_1 decreased in the 10%CF-$SrTiO_3$ compared to $SrTiO_3$ and 5%CF-$SrTiO_3$, which enhanced the ionic conduction at the Surface. Also, due to the thermal effect, the excess number of charges can move at the grain boundary of 10%CF-$SrTiO_3$. Also, the reduction of R_o causes the fast transportation of ions which in turn enhance the performance of the fuel cell device. The morphology and EIS are correlated in the case of particle connection at the nano and micro-level, leading to a massive network assisting in the fast charge transportation of ions at the Surface of the proposed composition. Also, uniform distribution and small particle size support better fuel cell and electrochemical performance by offering lower interfacial polarization resistance, as can be confirmed in Fig. 4. Instead of the above discussion, the thermal effect plays a crucial role in reducing the electrode polarization resistance R_p and ohmic resistance [36]. Fig. 4(b) shows the commercially available material $SrTiO_3$ while Fig. 4(e and f) shows the EIS spectra of 10%CF-$SrTiO_3$ & 5%CF-$SrTiO_3$ at 520 °C. Furthermore, detailed EIS analysis of CF-STO under different environments (CF-STO & STO under H_2/Air), CF-STO D_2 and CF-STO 5% H_2/Ar95% at 520 °C are presented in supporting documents (Fig SI. (7-10).

The fuel cell performance of the proposed composition and parent composition in terms of the I–V and I–P characteristics curve have been performed in H_2/Air environments at different operating temperatures, as seen in Fig. 5(a–c). The fabricated fuel cell device for pristine STO in the configuration of Ni-NCAL/$SrTiO_3$/NCAL-Ni has delivered a maximum power output of 492 mW/cm^2 (OCV of 1.08 V) at 520 °C, and 343 and 142 mW/cm^2 at 470 and 420 °C, respectively, as shown in Fig. 5 (a). While for CF-$SrTiO_3$ electrolyte fuel cell device of Ni-NCAL/5%CF-$SrTiO_3$/NCAL-Ni has delivered a maximum power output of 625, 444, and 338 mW/cm^2 at 520, 480, 470 °C, respectively, see Fig. 5(b). By optimizing CF-STO composition with 10% of Co/Fe surface doping, e.g., $SrCo_{0.1}Fe_{0.1}TiO_3$ as the electrolyte, the device has displayed an impressive performance of 1016, 696, and 429 mW/cm^2 with good OCV above 1.0 V at 520, 470, and 420 °C, respectively, as shown in Fig. 5(c). The remarkable enhancement of the fuel cell performances from 625

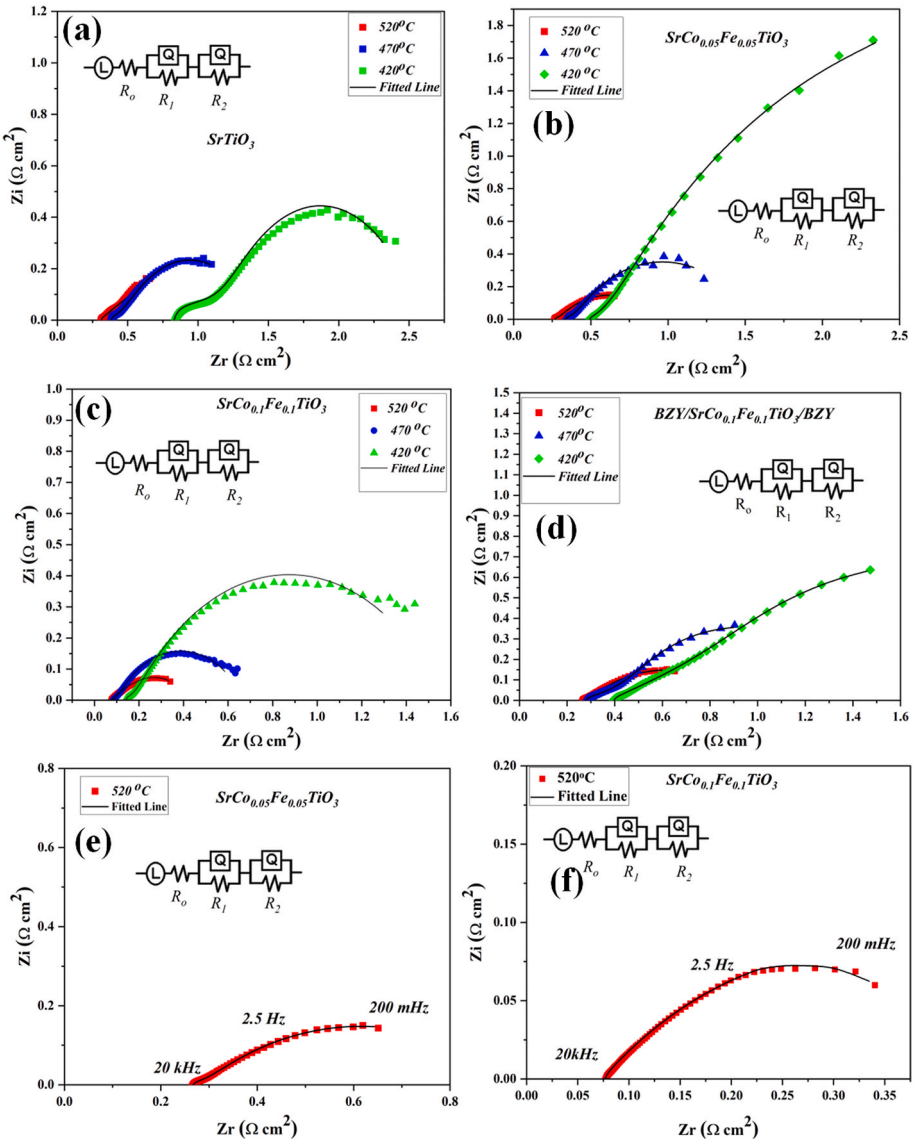

Fig. 4. (a–d) EIS spectra of $SrTiO_3$, 5%CF-$SrTiO_3$, 10%CF-$SrTiO_3$ and BZY/10%CF-$SrTiO_3$/BZY under H_2/Air environment and at different operational temperature 520-420 °C, while (e, f) EIS spectra of 5%CF-$SrTiO_3$ and 10%CF-$SrTiO_3$ at 520 °C.

mW to 1016 mW/cm^2 correlated to the 5% and 10% of Co/Fe surface doping into STO suggests that surface doping can effectively improve the STO electrical property and electrochemical performance. Such high performance is owed to surface doping and lower grain boundary resistance, as discussed in the above EIS analysis. The surficial doping approach may effectively create more active sites and fast-moving paths for ion transport on the Surface [14,17,23]. Also, surface doping influences the bandgap (energy band alignment), enhancing the electrical property and fuel cell performance. Also, the performance of 15% CF-$SrTiO_3$was tested under an identical environment and delivered a power output of 715 mW/cm^2 at 520 °C, which is lower than the 10% CF-$SrTiO_3$1016 mW/cm^2, suggesting 10%CF-$SrTiO_3$ is an optimal composition for better fuel cell performance as depicted in Fig. I11. Finally, higher device performances and good OCVs indicate that CF-STO, especially, 10%CF-$SrTiO_3$ is a competent electrolyte for fuel cell application. Moreover, three different cells have been tested under identical environments (H_2/Air at 520 °C) using 10%CF-STO as an electrolyte to reproduce the attained power output of 1016 mW/cm^2 displayed in the supporting documents (Fig.SI.12).

The attained power density via surface doping of 10%CF-$SrTiO_3$ is comparable to or even higher than the reported literature of SOFC-based electrolytes such as YSZ (Yttria stabilized zirconium), SDC (Samarium-doped Ceria), and BCZYY (BaCoZrYYb), SFT ($SrFeTiO_3$), $SrTiO_3$, La–$SrTiO_3$ under the identical operating condition, where electrolyte possesses the thickness of 0.7 mm [2,12,22,23,37,38]. Fig. 5(d) compares obtained power density between different compositions and parent materials. Also, the proposed device performance is slightly lower than the advanced thin film technology-based electrolyte like YSZ μ-SOFC. This might be due to the technological difference between macro and micro-scale SOFC [39]. The obtained results suggest that the adopted approach of surface doping has successfully been implemented with enhanced performance and could be a promising approach for advanced fuel cell technology.

Furthermore, to certify the proton conduction in the synthesized material CF-STO ($SrCo_{0.1}Fe_{0.1}TiO_3$) blocking layer such as BZY (which blocks the O^{2-} & e^-) only allows protons (H^+) to pass through the electrolyte layer CF-STO. So, the five-layer device was built in the following configuration (Ni-NCAL/BZY/10%CF-STO/BZY/NCAL-Ni) to determine the performance (IV/IP characteristic curve) under H_2 and Air environments at different operational temperatures of 520-420 °C. This five-layer technique has previously been performed to investigate the specific ionic species (protons conduction) and to filter the other

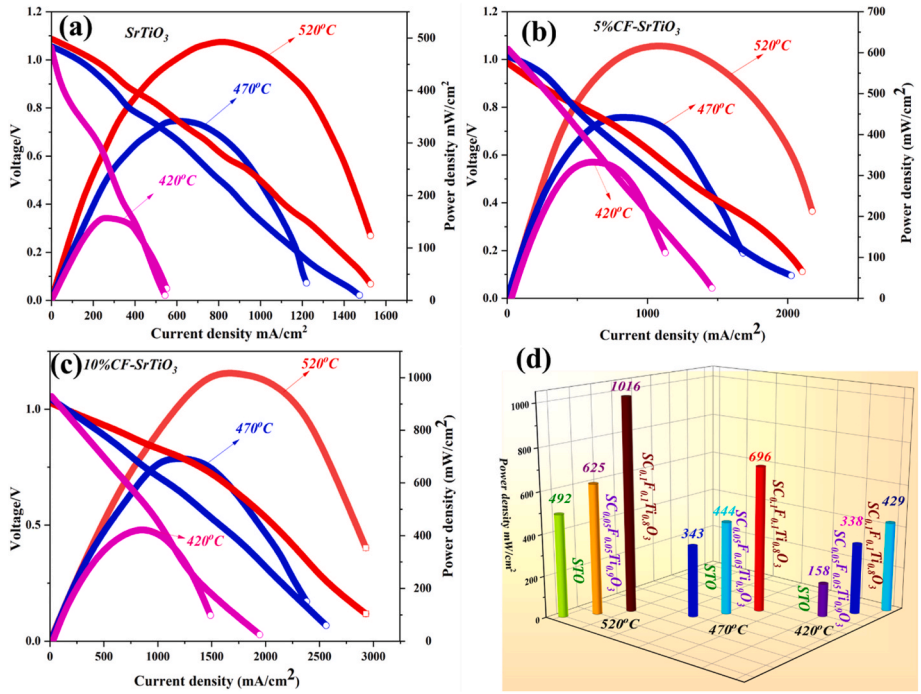

Fig. 5. (a–c) I–V/I–P characteristic curve of $SrTiO_3$, 5%CF-$SrTiO_3$ and 10%CF-$SrTiO_3$ under H_2/Air environment and at different operational temperatures 520-420 °C, while (d) comparison between $SrTiO_3$, 5%CF-$SrTiO_3$ and 10%CF-$SrTiO_3$ at different operational temperature 520-420 °C.

charge carriers simultaneously. BZY is reported as a proton conductor but with negligible other species, such as O and e, which can be used to investigate the proton's performance, and proton conductivity can be determined using the I–V curve as investigated in earlier reports [14,17, 30,40]. The constructed device performance was examined under identical environments, as shown in Fig. 6 (a). The five-layer device delivered an 800 mW/cm2 at 520 °C, 80% of the total performance (1016 mW/cm2), suggesting that the proposed device possesses dominant protons conduction. Furthermore, Fig. 6(b) shows the EIS spectra of five-layer device BZY/CF-ST-/BZY and CF-STO under H_2/Air, D_2 and H_2/Ar environment, exhibiting less resistance like lower resistance of ohmic and grain boundary, suggesting that ionic conduction (proton) is

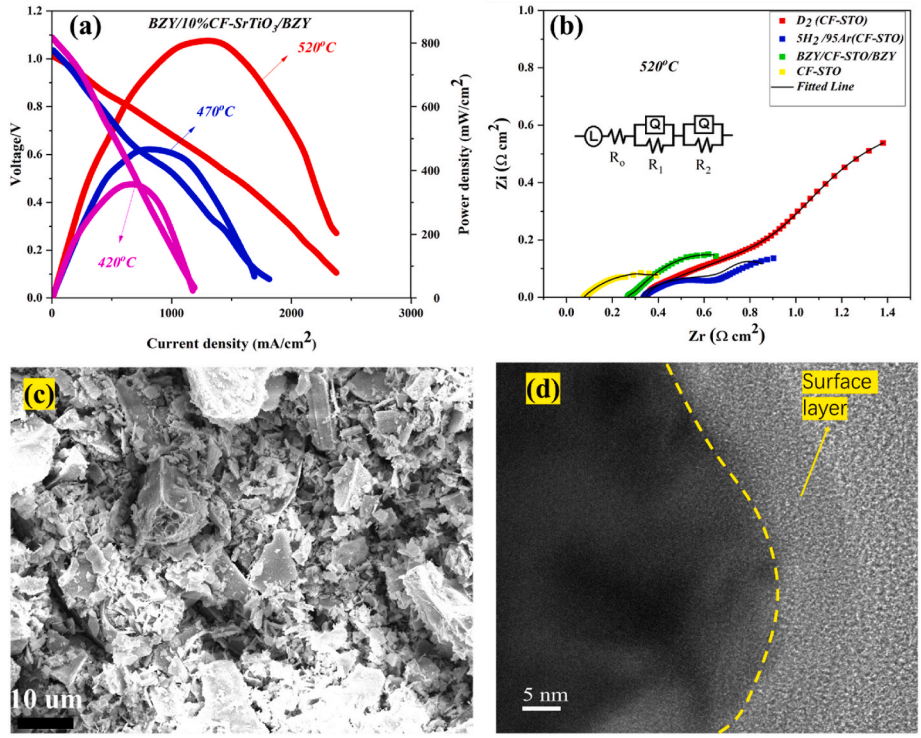

Fig. 6. (a) I–V/I–P characteristic curve of BZY/CF-$SrTiO_3$/BZY under H_2/Air environment and at different operational temperatures 520-420 °C, while (b) the EIS spectra of CF-$SrTiO_3$ under different environments like D_2, 95%Ar/5%H_2 and H_2/Air also BZY/CF-$SrTiO_3$/BZY EIS spectra under H_2/Air environment at 520 °C, (c, d) SEM image of BZY powder and HR-TEM image of CF-$SrTiO_3$ with a surface layer.

higher at the Surface and interface. Moreover, the phenomena of proton conduction have been explained in a later section. Furthermore, Fig. 6(c, d) exhibits the SEM image of BZY and the HR-TEM image of 10% CF-$SrTiO_3$, revealing the surface layer along with the core and interface, confirming the successful surface co-doping of Co/Fe into STO lattice.

The XPS (x-ray photoelectron spectroscopy) investigates the surface properties and chemical states. The characteristics of each element, including Sr, Co, Fe, Ti, O, and C, have been indicated in the whole spectra of XPS of proposed samples 10%CF-STO & 5%CF-STO as displayed in Fig. 7(a). The core-level spectra of all elements, including Sr-3d, Co-2p, Fe-2p, Ti-2p, and O-1s, have been discussed in detail to identify the chemical states. Also, each element has been deconvoluted into different peaks by applying the Gaussian function. The supplementary information has explained the other peak detail of the whole spectra, Sr-3d, Co-2p and Fe-2p, described in the supplementary information (Fig.SI13(a-e). Moreover, the XPS full spectra of $SrTiO_3$, and O-1s spectra and after testing XPS spectra of Co-2p, Fe-2p and O-1s of CF-STO have been presented in supporting information in Fig.SI 14(a, b) & 15(a-c).

The O-1s spectra have been deconvoluted into three peaks, O_α, O_β, and O_γ, as shown in Fig. 7 (e, f). O_α corresponds to the lattice oxygen, O_β correlates to the oxygen defects, while O_γ is attributed to the surface oxygen species. In detail, the binding energy of 528.8 eV–529.4 eV is ascribed to the lattice oxygen. In contrast, the binding energy of 531.0–532.6 eV is related to the oxygen defects and surface oxygen species, where the surface O-species are adsorbed on the O-vacancies (O^-, OH^- and CO_3^{2-}) [14,17,27,31]. The surface doping of the dopants to the host materials leads to the form of the Ti–O dopant bond, which enables the oxygen to be more liable to facilitate the migration or movement process of ions from the bulk lattice to the surface lattice leading to enhancing the surface conduction [23,31,41]. Also, the doping causes peak area has been improved, cluing to accommodate more oxygen species and oxygen vacancies, enhancing ionic conduction [16].

The above results have shown that based on the structural design, surface doping leads to establishing the enriched surface oxygen vacancies layer, which helps to enhance the ionic conductivity. Pure and commercially prepared $SrTiO_3$ has high bulk or grain boundary resistance because of the highly aligned structure, which bounds the motion of ions for easy transportation. In contrast, the Surface doped CF-$SrTiO_3$ sample owns the excess number of O-vacancies, especially at the Surface, and the interface helps to boost the ionic conduction. The heterojunction could be facilitated by establishing a surface layer with Co/Fe doping. Also, the ions can be manipulated via the interface of heterogenous same as the Ni–Sm_2O_3, $CeO_2/CeO_{2-\delta}$ and BCFZY-ZnO interfacial junction [14,17,30].

Moreover, the surface doping causes to reduces the bandgap from 3.26 to 2.88 eV in $SrCo_{0.1}Fe_{0.1}TiO_3$, which mainly assists in quick charge transportation via the intermediate states above and below the Fermi level, and such fast transport of charges influences the ionic conduction of proposed material as shown in Fig. 8(a and b). Also, the exact band edge position of the proposed material $SrCo_{0.1}Fe_{0.1}TiO_3$ and STO have been determined using the Uv–visible spectroscopy; also, the Uv of $SrTiO_3$ has been presented in the supplementary information. In comparison, the position of the valence band has been calculated by subtracting the cut-off energy of the 2ndary electron from the He = 21.2 eV (c, d). Also, the fermi level position has been shifted negatively upon Co and Fe surface doping in $SrTiO_3$, as shown in Fig. 8(e and f). The Uv–visible and UPS spectra of STO and CF-STO are shown in the supplementary Information (Fig. I16(a-d)).

The doping of Co and Fe causes a reduced bandgap revealing that Co and Fe orbital impurity energy levels are located above the valence band maximum also, the excitation energy of discovered defects in intermediate states to the conduction band got reduced, leading to the fact of appearing red shift in the absorption of CF-STO [17,24,25]. Moreover, Co/Fe co-doping altered the energy bands of STO. The tailed band energetics due to surface doping leads to the formation of homojunction (due to different fermi-level between STO & CF-STO), creating the depletion region at the interface of STO & CF-STO as displayed in Fig. 8 (g). The depletion zone involved the electron occupation at the CF-STO side, while the positive charge layer was placed at the STO site that neighbored the interface. The formation or established homo-junction probably triggers the kinetics of ions diffusion. Also, the depletion region constitutes the built-in field assisting ionic transportation, as depicted in Fig. 8(h) [42].

The above result clued that the proposed device based on CF-STO

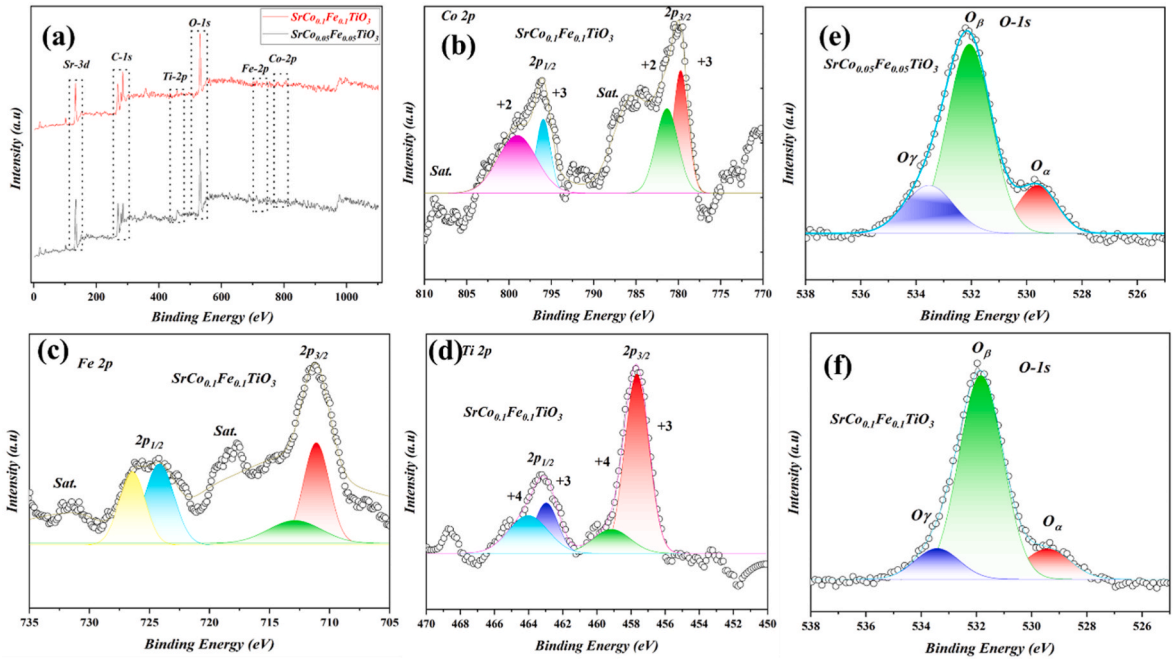

Fig. 7. (a) full XPS spectra of 5%CF-$SrTiO_3$ and 10%CF-$SrTiO_3$ while (b–d) the XPS spectra of Co, Fe and Ti, (e, f) O1-s Spectra of 5%CF-$SrTiO_3$ and 10%CF-$SrTiO_3$ respectively.

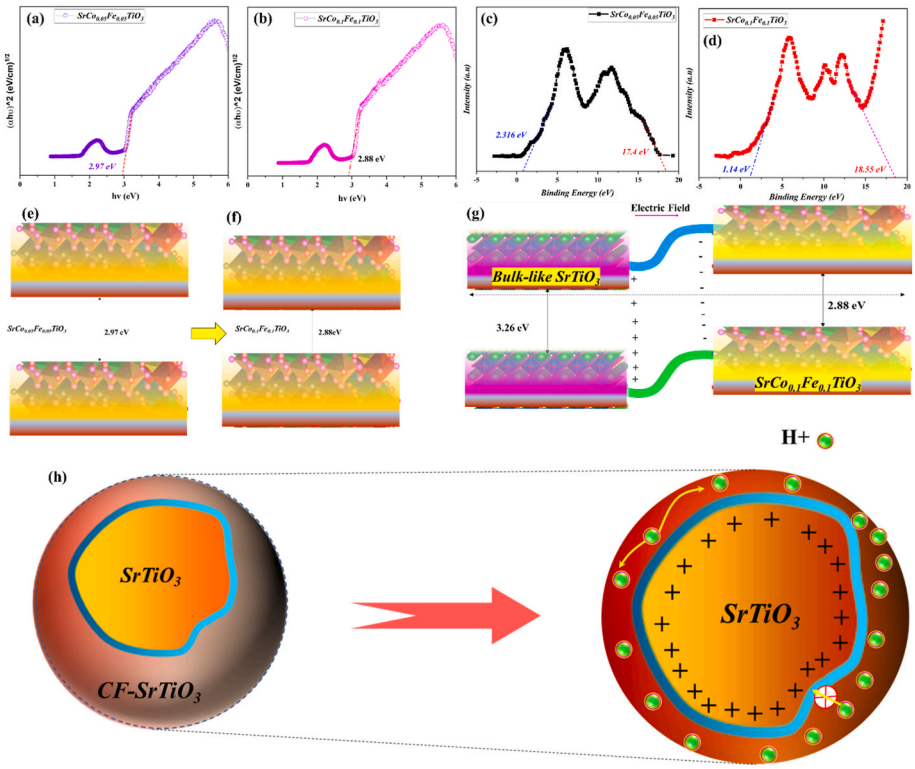

Fig. 8. (a–d) the Uv–visible (energy bandgap) and UPS spectra of 5%CF-$SrTiO_3$ and 10%CF-$SrTiO_3$, (e–g) energy bandgap diagram and energy band alignment between $SrTiO_3$ and 10%CF-$SrTiO_3$ (h) proton transport mechanism on the surface of CF-$SrTiO_3$.

electrolyte is competent in case of better performance and enriched surface conduction due to surface doping. Furthermore, to determine the ionic conductivity of CF-STO and STO, the CF-STO I–V curve of fuel cell performance is aimed where the central portion of the I–V curve manifests the ohmic polarization resistance corresponding to the ohmic polarization region [30]. The obtained resistance was used to calculate the ionic conduction by employing the following equation $\sigma = \frac{L}{R \times A}$ Where L represents the thickness of the electrolyte layer, which is about 0.75 μm, A is the Pellet area, and R is the ohmic resistance of the polarization region of the I–V curve. The obtained ionic conductivity of the proposed electrolyte $SrCo_{0.1}Fe_{0.1}Ti_{0.8}O_3$ is 0.19–0.077 S/cm at 520-420 °C. In contrast, the attained ionic conductivity 0.101–0.0234 S/cm and 0.139–0.0425 S/cm cross-ponds to the $SrTiO_3$ and $SrCo_{0.05}Fe_{0.05}Ti_{0.9}O_3$ at 520-420 °C respectively. Interestingly, the obtained ionic conductivity of $SrCo_{0.1}Fe_{0.1}Ti_{0.8}O_3$ is higher than the other composition and parent material ($SrCo_{0.05}Fe_{0.05}Ti_{0.9}O_3$ & $SrTiO_3$), suggesting that 10% surface doping is suitable enough to produce more O-vacancies suitable at the surface of lattice and finally enhance the ionic conductivity with minor electronic conduction. Also, the obtained ionic conductivity is higher than the reported literature under the same operating condition manifesting that $SrCo_{0.1}Fe_{0.1}Ti_{0.8}O_3$ is the competent electrolyte for low-temperature fuel cell technology [37,38].

The Hebb Vagner polarization method was used to calculate the electronic conductivity by recording the data between time and current with a fixed voltage of 1 V for half an hour at different operational temperatures 520-420 °C. The obtained electronic conductivity of the proposed or best composition is 0.00029 S/cm at 520 °C, which is negligible compared to high ionic conductivity. Such high ionic conductivity is owed to low grain boundary resistance because as the Co and Fe are doped in $SrTiO_3$ resistance of the proposed composition, significantly the grain boundary resistance got reduced, suggesting the creation of more O-vacancies on the Surface, resulting in enhanced ionic conduction and lower the activation energy of 0.5 eV. The activation energy of all prepared compositions and parent material has been determined using the following equation, and all parameters of the stated equation have been explained elsewhere [30]. The ionic conductivity and activation energy curve of all compositions have been shown in Fig. 9 (a, b). In contrast, the electronic conductivity and the polarization curve has been demonstrated in the supplementary information (Fig.SI (17, 18).

Furthermore, the disorder inspection and investigation of interactive variation in the structure of prepared materials have been performed using the Raman spectra. All samples, including STO, 5%CF-STO, and 10%CF-STO, have a pure cubic phase without any dominant impurity peak, as displayed in Fig. 1(a). Mostly, the 2nd order is prevalent in our prepared materials, while the first-order scattering is proportionally banned. The Raman spectra of 5%CF-STO and 10%CF-STO have been recorded in the range of Raman shift of 0–1000 cm^{-1} and at room temperature, as depicted in Fig. 9(c). In case of comparison, both Raman scattering of 5%CF-STO and 10%CF-STO are identical in shape to $SrTiO_3$ but wider and scattered to a long range which might attribute to the incorporation of Co and Fe into the lattice of $SrTiO_3$. Besides, some peaks of the first-order effect appear in CF-STO and STO symmetry which mainly cross-ponds to the bending mode of O–Sr–O, O–Ti–O, and stretching mode of Ti–O. Also, the broad range spectra (200–500 & 600-800 cm^{-1}) have been inspected in all samples, including STO and CF-STO. The broader spectra of CF-STO clue the successful incorporation in STO lattice. Also, the Raman spectra of SrTiO3 have been displayed in the supplementary information (Fig.SI. (19)).

DFT (density functional theory) was used to optimize the structure of 10%CF-STO, as shown in Fig. 9(d). After optimization, the structure shows the disorder in the lattice-like changes in the bond length and angle, which may lead to defects in the lattice and on the surface and increase the concentration of O-vacancies, enhancing the ionic conduction of the CF-STO lattice. The obtained O-Vacancy formation energy using the vacancy formation equation was 5.2 eV (where STO formation energy is 6.7 eV), according to the previous literature suggesting a higher concentration of O-vacancies [43,44]. The images before and

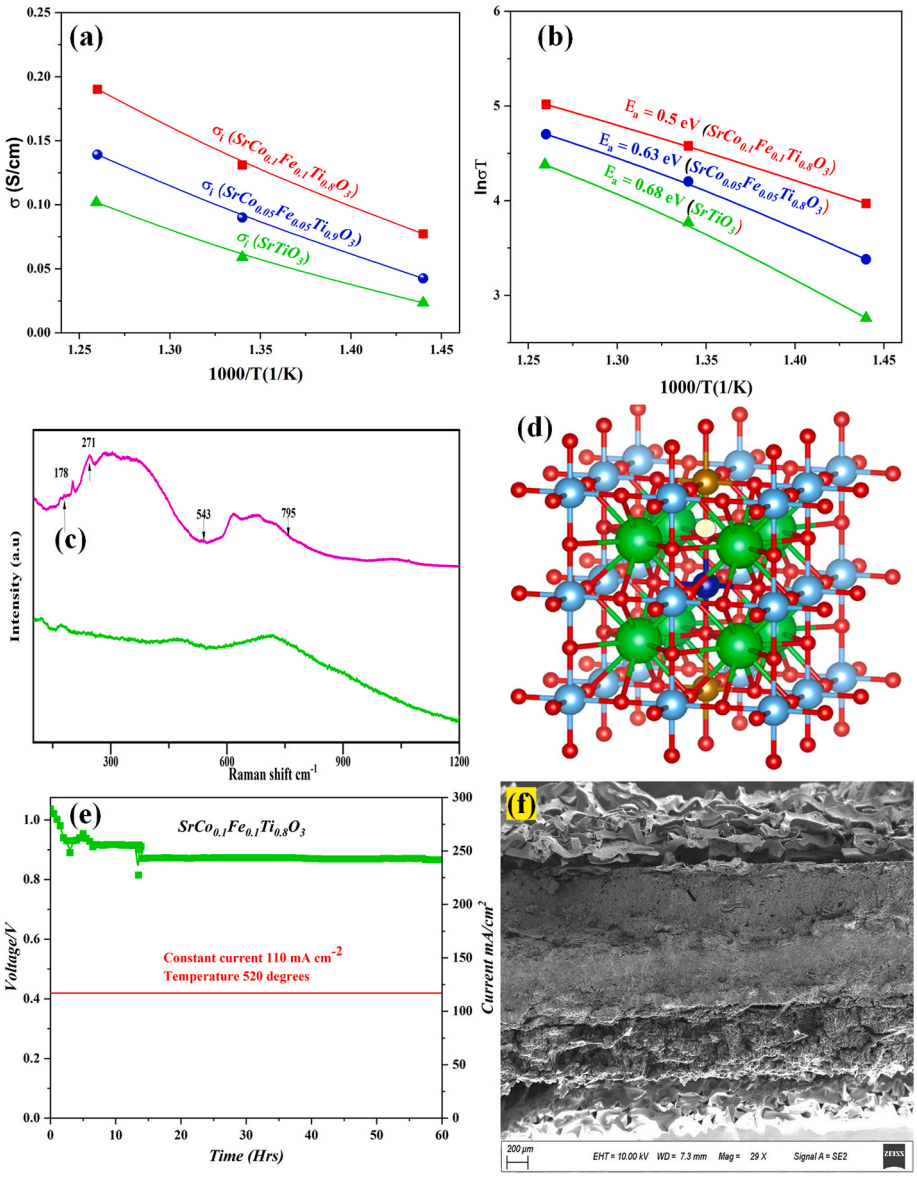

Fig. 9. (a, b) Ionic conductivity and activation energy of $SrTiO_3$, 5%CF-$SrTiO_3$ and 10%CF-$SrTiO_3$ (c) the Raman spectra of $SrTiO_3$ and 10%CF-$SrTiO_3$, (d) optimized structure of 10%CF-STO with oxygen vacancy (d, e) durability of 10%CF-$SrTiO_3$ under H_2/Air environment at 520 °C and cross-sectional view of Ni-NCAL/CF-$SrTiO_3$/NCAL-Ni after durability test.

after optimization with the bond lengths have been displayed in the supplementary information (Fig.SI (20–26).

The durability operation of the CF-STO electrolyte-based fuel cell has been performed at 520 °C in fuel-cell working conditions, as demonstrated in Fig. 9 (e). The cell stays stable for about 50 h at the OCV of 0.84 V with a steady current density of 110 mA/cm^2. In the initial stage of about 5 h, the OCV decreased smoothly. Then without any degradation, it reached a steady level of 0.84 V. The initial process of falling in stability might appear due to the activation of electrodes and the interface gap. When the electrode is activated and the gap minimized, and more importantly, protons injection into the CF-STO during the fuel cell operation to build up stable proton transport paths, leading to improved and durable proton conduction, the stead-stable process can be reached. Also, after 10 h abrupt decrease was due to a technical problem. Moreover, the SEM cross-sectional view of a cell after durability was tested, revealing the electrolyte is precisely sandwiched between symmetrical electrodes (Ni-NCAL/CF-STO/NCAL-Ni), as shown in Fig. 9(f). In the current laboratory test cells to demonstrate the CF-STO feasibility for the electrolyte, lacking engineering efforts to develop cell fabrication technology, there is a large room to improve the cell durability through further technical development.

4. Conclusions

In this work, STO is doped with transition elements, Co, and Fe, which built up a special surface charge region on the STO. This surface modification created paths for ion transports and promoted proton transport facilitated by the built-in electric field of the space charge region. Also, DFT calculations have verified that the doping disorder in lattice and the formation of oxygen vacancies assist high ions transportation. On the other hand, Co/Fe co-doping in STO could induce electronic conduction in it. However, an appropriate doping level resulted in fairly low electronic conduction (0.00029 S/cm) as compared to the ionic conduction (0.19 S/cm) making Co/Fe–$SrTiO_3$ as potential electrolyte material. The fuel cell utilizing this promising electrolyte produced a remarkable power density of 1016 mW/cm^2 at 520 °C demonstrating its successful application in CFCs.

Credit author contribution statement

Bin Zhu., M. Imran Asghar and Yu Zheng Lu Conceptualization the idea, designed the experiments, and analyzed the data. **M. A. K. Y. Shah** carried out synthesis, characterizations, theoretical calculation, paper write. **Naveed Mushtaq, Sajid Rauf and Yiwang Dong** carried out few characterizations and device optimizations. **M. Yousaf and M. Akbar** revised some parts of the manuscript and performed a stability test. **M. A. K. Y. Shah, Naveed Mushtaq, Bin Zhu, Peter. D Lund, M. Imran Asghar** participated in device optimization and data analysis. **M. Yousaf** analyzed the X.R.D results. **M. A. K. Y. Shah** verified fuel cell results. **M. A. K. Y. Shah, Bin Zhu** wrote the paper. All authors commented on the manuscript.

Declaration of competing interest

The authors declare that they have no known competing financial interests or personal relationships that could have appeared to influence the work reported in this paper.

Data availability

Data will be made available on request.

Acknowledgement

This work was supported by Southeast University (SEU) project3203002003A1 and National Natural Science Foundation of China (NSFC) under the grant 51772080 and 11604088. Jiangsu Provincial Innovation and Entrepreneurship Talent program Project No. JSSCRC2021491. Industry-University-Research Cooperation Project of Jiangsu Province in China, Grant No. BY2021057. Dr. Asghar thanks the Hubei Talent 100 program in China and the Academy of Finland (Grant no. 13329016, 13322738, 13352669) for their financial support.

Appendix A. Supplementary data

Supplementary data to this article can be found online at https://doi.org/10.1016/j.memsci.2022.121264.

References

[1] J. Cao, Y. Ji, Z. Shao, Perovskites for Protonic Ceramic Fuel Cells: a Review, Energy & Environmental Science, 2022.
[2] C. Duan, J. Tong, M. Shang, S. Nikodemski, M. Sanders, S. Ricote, A. Almansoori, R. O'Hayre, Readily processed protonic ceramic fuel cells with high performance at low temperatures, Science 349 (6254) (2015) 1321–1326.
[3] Y.-Y. Chen, W.-C.J. Wei, Processing and characterization of ultra-thin yttria-stabilized zirconia (YSZ) electrolytic films for SOFC, Solid State Ionics 177 (3–4) (2006) 351–357.
[4] J.B. Goodenough, Oxide-ion conductors by design, Nature 404 (6780) (2000) 821–823.
[5] K. Kerman, B.K. Lai, S. Ramanathan, Nanoscale compositionally graded thin-film electrolyte membranes for low-temperature solid oxide fuel cells, Adv. Energy Mater. 2 (6) (2012) 656–661.
[6] B.C. Steele, A. Heinzel, Materials for Fuel-Cell Technologies, Materials for Sustainable Energy: a Collection of Peer-Reviewed Research and Review Articles from Nature Publishing Group, World Scientific2011, pp. 224-231.
[7] K. Bae, D.Y. Jang, H.J. Choi, D. Kim, J. Hong, B.-K. Kim, J.-H. Lee, J.-W. Son, J. H. Shim, Demonstrating the potential of yttrium-doped barium zirconate electrolyte for high-performance fuel cells, Nat. Commun. 8 (1) (2017) 1–9.
[8] S.V. Bhide, A.V. Virkar, Stability of BaCeO3-based proton conductors in water-containing atmospheres, J. Electrochem. Soc. 146 (6) (1999) 2038.
[9] K.-D. Kreuer, Proton-conducting oxides, Annu. Rev. Mater. Res. 33 (1) (2003) 333–359.
[10] W. Sun, Z. Shi, M. Liu, L. Bi, W. Liu, An easily sintered, chemically stable, barium zirconate-based proton conductor for high-performance proton-conducting solid oxide fuel cells, Adv. Funct. Mater. 24 (36) (2014) 5695–5702.
[11] R. Lan, S. Tao, Novel proton conductors in the layered oxide material LixlAl0. 5Co0. 5O2, Adv. Energy Mater. 4 (7) (2014), 1301683.
[12] G. Chen, H. Liu, Y. He, L. Zhang, M.I. Asghar, S. Geng, P.D. Lund, Electrochemical mechanisms of an advanced low-temperature fuel cell with a SrTiO 3 electrolyte, J. Mater. Chem. 7 (16) (2019) 9638–9645.
[13] Y. Zhou, X. Guan, H. Zhou, K. Ramadoss, S. Adam, H. Liu, S. Lee, J. Shi, M. Tsuchiya, D.D. Fong, Strongly correlated perovskite fuel cells, Nature 534 (7606) (2016) 231–234.
[14] Y. Xing, Y. Wu, L. Li, Q. Shi, J. Shi, S. Yun, M. Akbar, B. Wang, J.-S. Kim, B. Zhu, Proton shuttles in CeO2/CeO2− δ core–shell structure, ACS Energy Lett. 4 (11) (2019) 2601–2607.
[15] B. Wang, B. Zhu, S. Yun, W. Zhang, C. Xia, M. Afzal, Y. Cai, Y. Liu, Y. Wang, H. Wang, Fast ionic conduction in semiconductor CeO2-δ electrolyte fuel cells, NPG Asia Mater. 11 (1) (2019) 1–12.
[16] W. Dong, Y. Tong, B. Zhu, H. Xiao, L. Wei, C. Huang, B. Wang, X. Wang, J.-S. Kim, H. Wang, Semiconductor TiO 2 thin film as an electrolyte for fuel cells, J. Mater. Chem. 7 (28) (2019) 16728–16734.
[17] F. Wang, E. Hu, H. Wu, M. Yousaf, Z. Jiang, L. Fang, J. Wang, J.S. Kim, B. Zhu, Surface-engineered homostructure for enhancing proton transport, Small Methods 6 (1) (2022), 2100901.
[18] B. Zhu, L. Fan, N. Mushtaq, R. Raza, M. Sajid, Y. Wu, W. Lin, J.-S. Kim, P.D. Lund, S. Yun, Semiconductor electrochemistry for clean energy conversion and storage, Electrochemical Energy Reviews 4 (4) (2021) 757–792.
[19] M.Y. Shah, Y. Lu, N. Mushtaq, M. Singh, S. Rauf, M. Yousaf, B. Zhu, ZnO/MgZnO Heterostructure Membrane with Type II Band Alignment for Ceramic Fuel Cells, 2022.
[20] S. Patial, V. Hasija, P. Raizada, P. Singh, A.A.P.K. Singh, A.M. Asiri, Tunable photocatalytic activity of SrTiO3 for water splitting: strategies and future scenario, J. Environ. Chem. Eng. 8 (3) (2020), 103791.
[21] M. Zhang, P.A. Salvador, G.S. Rohrer, Influence of Particle Size and Shape on the Rate of Hydrogen Produced by Al-doped SrTiO3 Photocatalysts, Journal of the American Ceramic Society, 2022.
[22] G. Chen, B. Zhu, H. Deng, Y. Luo, W. Sun, H. Liu, W. Zhang, X. Wang, Y. Qian, X. Hu, Advanced fuel cell based on perovskite La–SrTiO3 semiconductor as the electrolyte with superoxide-ion conduction, ACS Appl. Mater. Interfaces 10 (39) (2018) 33179–33186.
[23] M.Y. Shah, Y. Lu, N. Mushtaq, S. Rauf, M. Yousaf, M.I. Asghar, P.D. Lund, B. Zhu, Demonstrating the potential of iron-doped strontium titanate electrolyte with high-performance for low temperature ceramic fuel cells, Renew. Energy 196 (2022) 901–911.
[24] M.Y. Shah, S. Rauf, N. Mushtaq, Z. Tayyab, N. Ali, M. Yousaf, Y. Xing, M. Akbar, P. D. Lund, C.P. Yang, Semiconductor Fe-doped SrTiO3-δ perovskite electrolyte for low-temperature solid oxide fuel cell (LT-SOFC) operating below 520° C, Int. J. Hydrogen Energy 45 (28) (2020) 14470–14479.
[25] M.Y. Shah, S. Rauf, B. Zhu, N. Mushtaq, M. Yousaf, P.D. Lund, C. Xia, M.I. Asghar, Semiconductor Nb-doped SrTiO3− δ perovskite electrolyte for a ceramic fuel cell, ACS Appl. Energy Mater. 4 (1) (2021) 365–375.
[26] M.Y. Shah, Z. Tayyab, S. Rauf, M. Yousaf, N. Mushtaq, M.A. Imran, P.D. Lund, M. I. Asghar, B. Zhu, Interface engineering of bi-layer semiconductor SrCoSnO3-δ-CeO2-δ heterojunction electrolyte for boosting the electrochemical performance of low-temperature ceramic fuel cell, Int. J. Hydrogen Energy 46 (68) (2021) 33969–33977.
[27] S. Rauf, B. Zhu, M. Yousaf Shah, Z. Tayyab, S. Attique, N. Ali, N. Mushtaq, B. Wang, C. Yang, M.I. Asghar, Application of a triple-conducting heterostructure electrolyte of Ba0. 5Sr0. 5Co0. 1Fe0. 7Zr0. 1Y0. 1O3− δ and Ca0. 04Ce0. 80Sm0. 16O2− δ in a high-performance low-temperature solid oxide fuel cell, ACS Appl. Mater. Interfaces 12 (31) (2020) 35071–35080.
[28] J. Garcia-Barriocanal, A. Rivera-Calzada, M. Varela, Z. Sefrioui, E. Iborra, C. Leon, S.J. Pennycook, J. Santamaria, Colossal ionic conductivity at interfaces of epitaxial ZrO2: Y2O3/SrTiO3 heterostructures, Science 321 (5889) (2008) 676–680.
[29] Y. Cai, Y. Chen, M. Akbar, B. Jin, Z. Tu, N. Mushtaq, B. Wang, X. Qu, C. Xia, Y. Huang, A bulk-heterostructure nanocomposite electrolyte of Ce0. 8Sm0. 2O2-δ–SrTiO3 for low-temperature solid oxide fuel cells, Nano-Micro Lett. 13 (1) (2021) 1–14.
[30] C. Xia, Y. Mi, B. Wang, B. Lin, G. Chen, B. Zhu, Shaping triple-conducting semiconductor BaCo0. 4Fe0. 4Zr0. 1Y0. 1O3-δ into an electrolyte for low-temperature solid oxide fuel cells, Nat. Commun. 10 (1) (2019) 1–9.
[31] N. Mushtaq, Y. Lu, C. Xia, W. Dong, B. Wang, M.Y. Shah, S. Rauf, M. Akbar, E. Hu, R. Raza, Promoted electrocatalytic activity and ionic transport simultaneously in dual functional Ba0. 5Sr0. 5Fe0. 8Sb0. 2O3-δ-Sm0. 2Ce0. 8O2-δ heterostructure, Appl. Catal. B Environ. 298 (2021), 120503.
[32] J. Jing, Z. Lei, Z. Wu, Z. Wang, H. Yu, Z. Yang, S. Peng, Ba0. 95La0. 05Fe0. 8Ni0. 2O3− δ Perovskite as Efficient Cathode Electrocatalysts for Proton-Conducting Solid Oxide Fuel Cells, Journal of the European Ceramic Society, 2022.
[33] N. Mushtaq, Y. Lu, C. Xia, W. Dong, B. Wang, X. Wang, M.Y. Shah, S. Rauf, N. Jingjing, E. Hu, Design principle and assessing the correlations in Sb-doped Ba0. 5Sr0. 5FeO3–δ perovskite oxide for enhanced oxygen reduction catalytic performance, J. Catal. 395 (2021) 168–177.
[34] Y. He, L. Zhang, Y. Wei, X. Zhang, Z. Wang, R. Yu, Semicrystalline SrTiO3-decorated anatase TiO2 nanopie as heterostructure for efficient photocatalytic hydrogen evolution, Small Methods 6 (3) (2022), 2101567.
[35] X. Chen, S. Zhan, D. Chen, C. He, S. Tian, Y. Xiong, Grey Fe-CeO2-σ for boosting photocatalytic ozonation of refractory pollutants: roles of surface and bulk oxygen vacancies, Appl. Catal. B Environ. 286 (2021), 119928.
[36] B. Zhu, R. Raza, L. Fan, C. Sun, Solid Oxide Fuel Cells: from Electrolyte-Based to Electrolyte-free Devices, John Wiley & Sons2020.
[37] D. Saebea, S. Authayanun, Y. Patcharavorachot, N. Chatrattanawet, A. Arpornwichanop, Electrochemical performance assessment of low-temperature solid oxide fuel cell with YSZ-based and SDC-based electrolytes, Int. J. Hydrogen Energy 43 (2) (2018) 921–931.

[38] L. Zhao, X. Huang, R. Zhu, Z. Lu, W. Sun, Y. Zhang, X. Ge, Z. Liu, W. Su, Optimization on technical parameters for fabrication of SDC film by screen-printing used as electrolyte in IT-SOFC, J. Phys. Chem. Solid. 69 (8) (2008) 2019–2024.
[39] H. Huang, M. Nakamura, P. Su, R. Fasching, Y. Saito, F.B. Prinz, High-performance ultrathin solid oxide fuel cells for low-temperature operation, J. Electrochem. Soc. 154 (1) (2006) B20.
[40] W. Zhang, Y.H. Hu, Progress in proton-conducting oxides as electrolytes for low-temperature solid oxide fuel cells: from materials to devices, Energy Sci. Eng. 9 (7) (2021) 984–1011.
[41] M.Y. Shah, Y. Lu, N. Mushtaq, M. Yousaf, S. Rauf, M.I. Asghar, P.D. Lund, B. Zhu, Perovskite Al-SrTiO 3 Semiconductor Electrolyte with Superionic Conduction in Ceramic Fuel Cells, Sustainable Energy & Fuels, 2022.
[42] W. Li, Q. Song, M. Li, Y. Yuan, J. Zhang, N. Wang, Z. Yang, J. Huang, J. Lu, X. Li, Chemical heterointerface engineering on hybrid electrode materials for electrochemical energy storage, Small Methods 5 (8) (2021), 2100444.
[43] V. Alexandrov, E. Kotomin, J. Maier, R. Evarestov, First-principles study of bulk and surface oxygen vacancies in SrTiO3 crystal, Eur. Phys. J. B 72 (1) (2009) 53–57.
[44] U.S. Shenoy, D.K. Bhat, Electronic structure engineering of SrTiO3 via rhodium doping: a DFT study, J. Phys. Chem. Solid. 148 (2021), 109708.